Co- and Early Postseismic Deformation Due to the 2019 Ridgecrest Earthquake Sequence Constrained by Sentinel-1 and COSMO-SkyMed SAR Data

Kang Wang[*1] and Roland Bürgmann[1]

Abstract

The 2019 Ridgecrest earthquake sequence ruptured a series of conjugate faults in the broad eastern California shear zone, north of the Mojave Desert in southern California. The average spacing between Global Navigation Satellite System (GNSS) stations around the earthquakes is 20–30 km, insufficient to constrain the rupture details of the earthquakes. Here, we use Sentinel-1 and COSMO-SkyMed (CSK) Synthetic Aperture Radar data to derive the high-resolution coseismic and early postseismic surface deformation related to the Ridgecrest earthquake sequence. Line of sight (LoS) Interferometric Synthetic Aperture Radar displacements derived from both Sentinel-1 and CSK data are in good agreement with GNSS measurements. The maximum coseismic displacement occurs near the M_w 7.1 epicenter, with an estimated fault offset of ∼4.5 m on a northwest-striking rupture. Pixel tracking analysis of CSK data also reveals a sharp surface offset of ∼1 m on a second northwest-striking fault strand on which the M_w 6.4 foreshock likely nucleated, which is located ∼2–3 km east of the major rupture. The lack of clear surface displacement across this fault segment during the M_w 6.4 event suggests this fault might have ruptured twice, with more pronounced and shallow slip during the M_w 7.1 mainshock. Both Sentinel-1 and CSK data reveal clear postseismic deformation following the 2019 Ridgecrest earthquake sequence. Cumulative postseismic deformation near the M_w 7.1 epicenter ∼2 months after the mainshock reaches ∼5 cm along the satellites' LoSs. The observed postseismic deformation near the fault is indicative of both afterslip and poroelastic rebound. We provide data derived in this study in various data formats, which will be useful for the broad community studying this earthquake sequence.

Introduction

On 4 July 2019, an M_w 6.4 earthquake struck the Searles Valley, near the town of Ridgecrest in southern California. The M_w 6.4 earthquake was followed by an M_w 7.1 event that took place about 34 hr later. Reports from field surveys and satellite imagery, including Interferometric Synthetic Aperture Radar (InSAR) and optical images, indicate a complex network of faults activated by the 2019 Ridgecrest earthquakes (Ross *et al.*, 2019). To understand the rupture process, the interactions between the two large events, and the associated stress changes on the regional fault system, detailed fault-slip models are necessary. High precision and resolution geodetic data are essential for this effort.

As part of the Plate Boundary Observation (PBO) project, thousands of continuous Global Navigation Satellite System (GNSS) stations are deployed across much of the western United States, providing near-real-time 3D measurements of surface movement across the Pacific-North American plate boundary at an accuracy of subcentimeter level. Despite their high accuracy and temporal resolution, GNSS measurements generally have poor spatial coverage and low-spatial resolution, due to the overall high cost of installation and maintenance. For PBO, the current average spacing between GNSS stations is 20–30 km in California, which is comparable to the rupture length of the 2019 Ridgecrest earthquake. In addition, temporally sparse campaign GNSS measurements help fill in some of the gaps in the coverage (e.g., Floyd *et al.*, 2019). Measurements of surface deformation at such a spatial resolution are useful to characterize the overall rupture process, but they are

1. Department of Earth and Planetary Sciences, University of California, Berkeley, California, U.S.A.

*Corresponding author: kwang@seismo.berkeley.edu

insufficient to reliably constrain the details of the rupture sequence. For example, they cannot account for the subsurface slip distribution or slip on secondary fault strands, which are important for understanding the stress interactions between the M_w 6.4 foreshock and the M_w 7.1 mainshock and their effects on nearby faults.

Spaceborne Synthetic Aperture Radar (SAR) measures the phase and amplitude of reflecting targets at a spatial resolution of a few meters, over a wide area. It is therefore ideal to study the ground deformation related to tectonic and nontectonic processes, including earthquakes, volcanoes, landslides, and land subsidence (Bürgmann et al., 2000). Here, we document the co- and early postseismic surface deformation, due to the 2019 Ridgecrest earthquake sequence, derived from Sentinel-1 and COSMO-SkyMed (CSK) SAR data. For data from both sensors, we derive the coseismic line of sight (LoS) displacements with conventional InSAR methods. We correct for various potential error sources (e.g., unwrapping errors and elevation-dependent atmospheric artifacts), and then we compare the results with GNSS observations to ensure that there are no systematic errors in our InSAR data. For the CSK data, we also derive the coseismic displacement along the azimuth direction of the satellite paths, using a pixel tracking technique (e.g., Fialko et al., 2001). We provide the data products in various formats, including the high-resolution grid data in Network Common Data Form (NetCDF) and Geographic Tagged Image File Format (GeoTiff), as well as deliberately downsampled ASCII files that can be directly used for coseismic slip modeling and other analyses (see Data and Resources). This article is complementary to several other contributions in this volume that focus on space geodetic observations. Specifically, Xu and Sandwell (2019) use Sentinel-1 InSAR to map the overall deformation field and focus on phase gradients associated with the small-scale fractures that are associated with 2019 Ridgecrest earthquake sequence. Fielding et al. (2019) report the surface deformation of the earthquake sequence with additional Advanced Land Observation Satellite-2 data (ALOS-2). Milliner and Donnellan (2019) present a unique dataset of surface deformation due to both the M_w 6.4 and the M_w 7.1 events using PlanetLab optical imagery. Floyd et al. (2019) present GNSS measurements collected immediately after the M_w 6.4 foreshock on 4 July, which will be essential to constrain the rupture process of the M_w 6.4 foreshock. In our article, in addition to the coseismic Sentinel-1 observations that are also considered in Xu and Sandwell (2019) and Fielding et al. (2019), we also include the LoS displacement and azimuthal offset measurements that were derived from the X-band CSK data, as well as early postseismic deformation measurements derived from both Sentinel-1 and CSK data. The high-resolution X-band CSK data allow us to derive detailed maps of surface deformation due to the Ridgecrest earthquake sequence along the satellite's flying direction, complementing the InSAR phase measurements along the LoS.

Data and Methods
C-band Sentinel-1

The epicentral area of the 2019 Ridgecrest earthquake is covered by two Sentinel-1 satellite tracks; these would be ascending track A064 and descending track D071 (Fig. 1). Both tracks had the last pre-earthquake image acquisitions hours before the 4 July 2019 M_w 6.4 earthquake (∼18 : 51 PDT 3 July for ascending track A064 and ∼06 : 52 PDT 4 July for descending track D071). The first postseismic acquisitions along the ascending track T064 and the descending track T071 were on UTC 10 July (∼18 : 51 on 9 July PDT), and 16 July (∼06 : 52 16 July PDT), respectively. Unfortunately, no images were acquired in between the M_w 6.4 foreshock and the M_w 7.1 mainshock. Subsequent acquisitions were made at six-day intervals, and we include observations up through 2 September 2019 in our data compilation that documents early postseismic deformation.

Orbital control of the Sentinel-1 satellites is so good that the geometric baseline between any two paths is generally smaller than 200 m, well below the critical value for C-band interferometry. To reduce the contribution from potential postseismic deformation, we form the coseismic interferograms using images acquired closest to the earthquake. We process the data using GMTSAR (Sandwell et al., 2011). The images of each track are aligned to a single master with geometrical alignment (Xu et al., 2017). We use the 1 arcsec (∼30 m ground resolution) Shuttle Radar Topography Mission digital elevation model for the image alignment and removal of topographic phase. We filter the real and imaginary parts of the original interferometric phase using a low-pass Gaussian filter with a 0.5 gain at a wavelength of 90 m. We unwrap the phase using Statistical-Cost Network-Flow Algorithm for Phase Unwrapping (SNAPHU) (Chen and Zebker, 2001), after masking out the pixels with a correlation that is smaller than 0.1.

Because of the lack of thick vegetation and the arid to semi-arid climate in southern California, the 2019 Ridgecrest earthquake area is characterized by generally high-radar coherence. Except for places very close to the rupture, where ground shaking is so strong that the reflection properties of the radar backscatters have been altered, the C-band Sentinel-1 phases remain well-correlated throughout the region, allowing for robust phase unwrapping. We visually check the unwrapped interferograms to ensure that there are no obvious phase jumps across neighboring patches of high-phase correlation. Because of the intrinsic ambiguity of phase unwrapping, the unwrapped interferograms may contain a constant shift. Because the Sentinel-1 scenes cover a larger area that contains the 2019 Ridgecrest earthquake, we flatten the unwrapped interferograms by fitting a polynomial function to the phase at pixels >80 km away from the epicenter of the M_w 7.1 earthquake, where the ground deformation due to the earthquakes is expected to be small. The resulting InSAR LoS displacements are in good agreement with the GNSS measurements derived from daily solutions
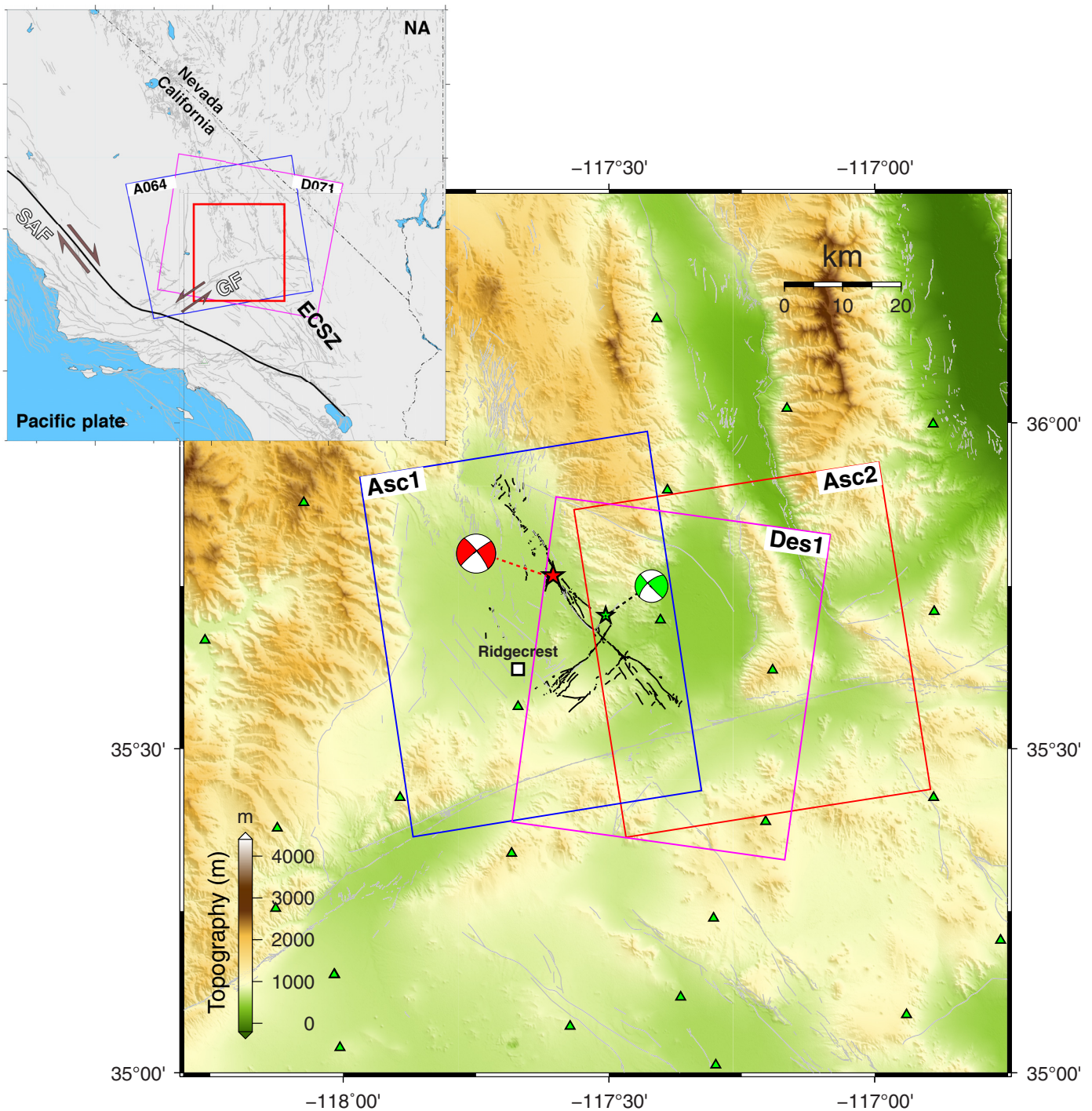
Figure 1. Ground coverage of Interferometric Synthetic Aperture Radar (InSAR) observations for the 2019 Ridgecrest earthquake sequence. The colored boxes denote the footprints of the COSMO-SkyMed (CSK) observations. Sentinel-1 scenes are shown in the inset map. Black lines show the surface traces of the 2019 Ridgecrest rupture sequence (D. Ponti *et al.*, unpublished manuscript, 2019, see Data and Resou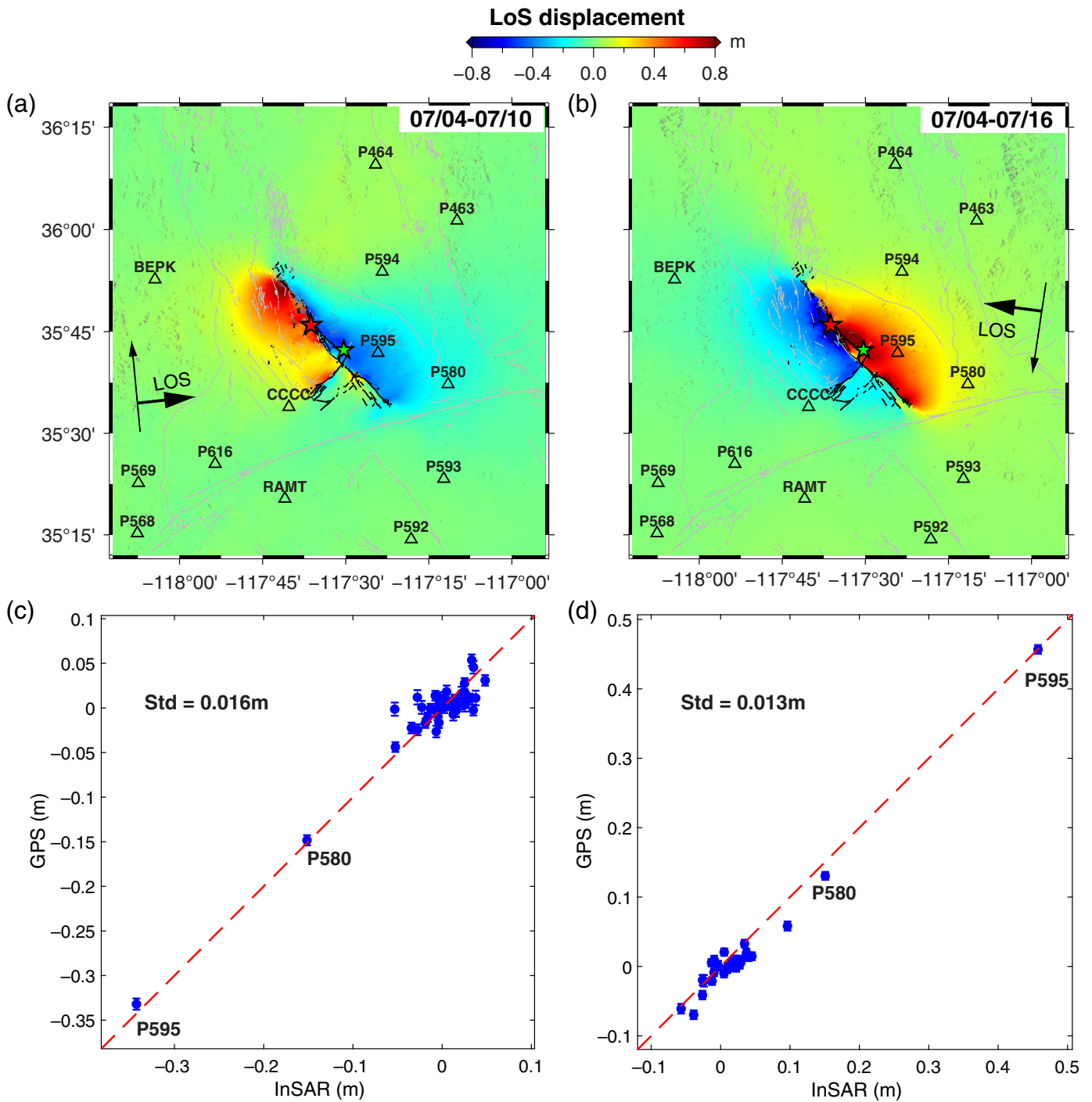rces). Green and red stars denote the epicenters of the M_w 6.4 foreshock on 4 July and the M_w 7.1 mainshock on 5 July, respectively. Green triangles represent the Plate Boundary Observation (PBO) continuous Global Navigation Satellite System (GNSS) stations. Inset shows the overall tectonic setting of the 2019 Ridgecrest earthquake. ECSZ, eastern California shear zone; GF, Garlock fault; SAF, San Andreas fault. The color version of this figure is available only in the electronic edition.

(Fig. 2). The standard deviation between InSAR and GNSS displacements projected onto the LoS is 1.6 and 1.3 cm for the ascending track A064 and descending track D071, respectively.

X-band CSK

Several CSK satellite tracks traverse the 2019 Ridgecrest earthquake area. However, compared to the Sentinel-1 wide-swath
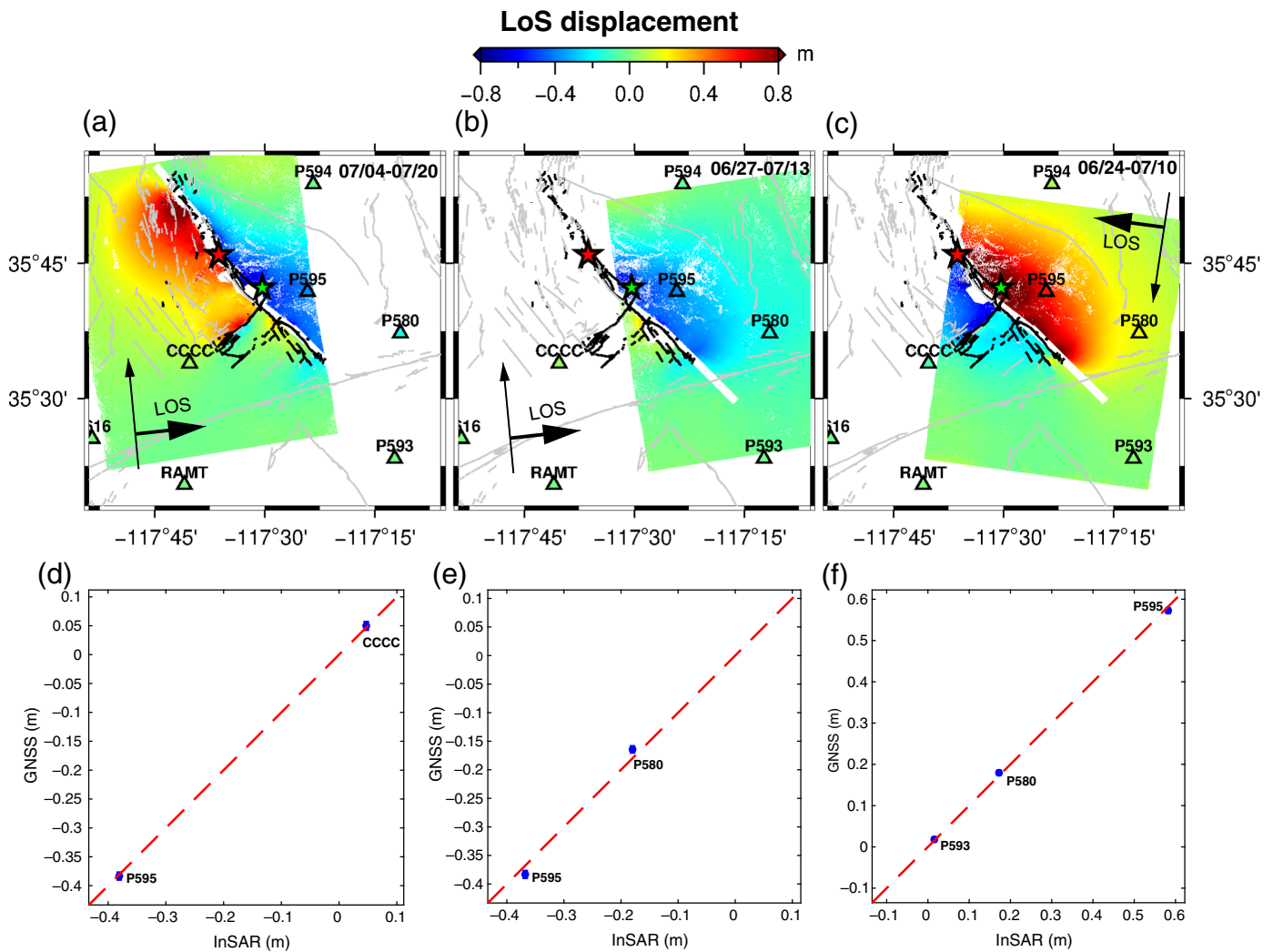
Figure 2. Coseismic line of sight (LoS) displacements due to the 2019 Ridgecrest earthquake sequence derived from Sentinel-1 data along the (a) ascending track A064 and (b) descending track D071. Triangles represent continuous GNSS stations of the PBO network, color coded by their 3D coseismic displacements that are projected onto the InSAR LoS. The InSAR and GNSS LoS displacements are shown with the same color scale. Text labels in the top right denote the dates of image acquisitions (UTC). The comparison between InSAR and GNSS LoS displacements is shown in (c) and (d) for track A064 and D071, respectively. Red dashed lines have slopes of one. The color version of this figure is available only in the electronic edition.
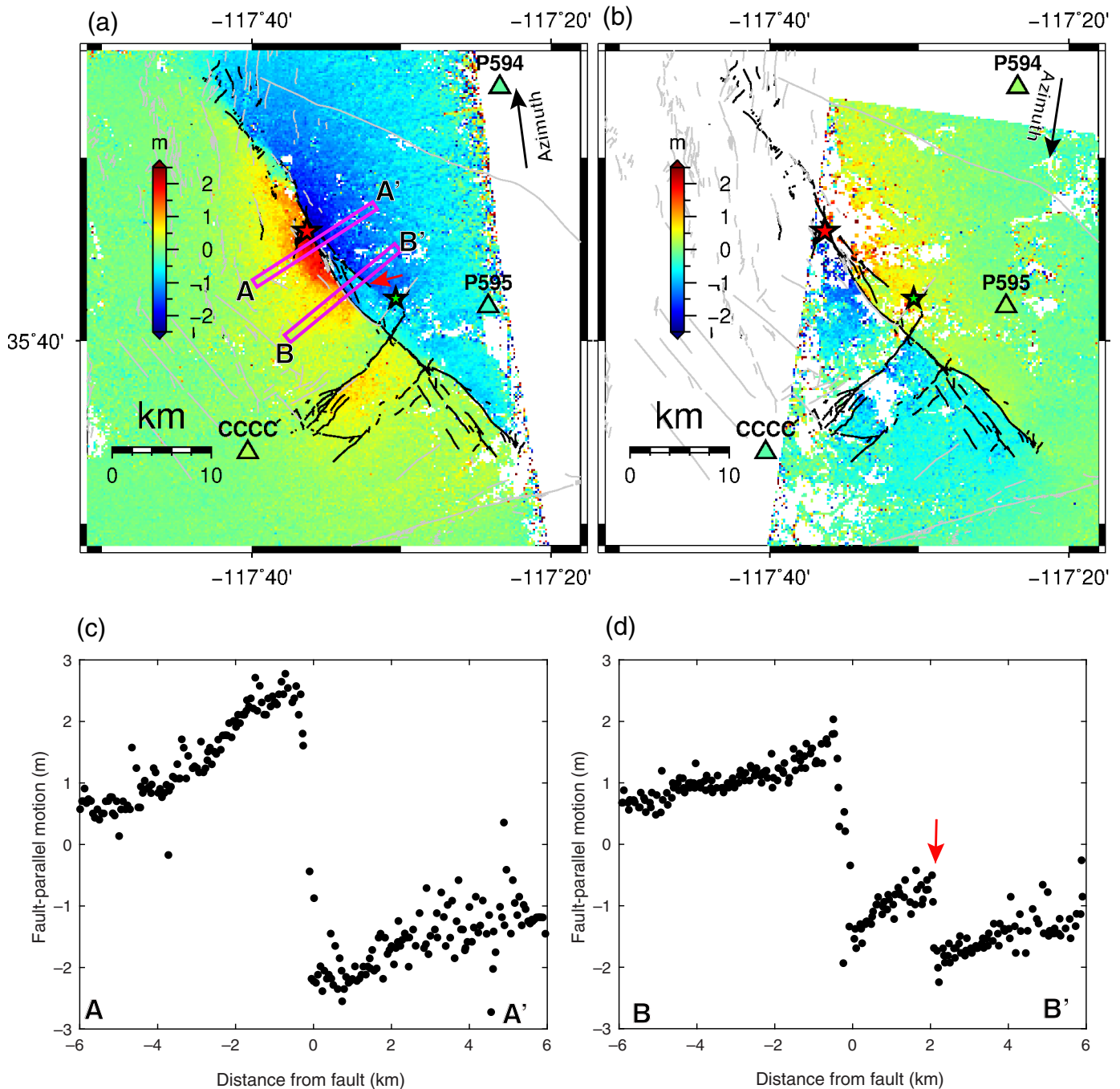
Terrain Observation with Progressive Scans SAR observations, the strip-mode CSK scenes have much narrower ground coverages (∼50 km wide), and each track covers only part of the rupture (Fig. 1). Similar to the processing of Sentinel-1 data, instead of using the GMTSAR built-in method of cross-correlating images to find the shift and stretch parameters between images for alignment, we align the CKS images using geometric alignment (Wang *et al.*, 2019).

Because of its short radar wavelength (∼3.1 cm), the phase gradients of the coseismic CSK interferograms are very high, which poses challenges to phase unwrapping for pixels near

Figure 3. LoS displacements due to the 2019 Ridgecrest earthquake sequence derived from CSK data along the ascending tracks (a) Asc1 and (b) Asc2 and the descending track (c) Des1. (d–f) Show comparison between InSAR observations and GNSS displacements projected onto the LoS of corresponding SAR acquisitions. Symbol notations are the same as in Figure 2. The color version of this figure is available only in the electronic edition.

the fault. We notice that unwrapping using SNAPHU with deformation mode sometimes produces phase jumps in areas close to the fault, where the phase correlation is generally low. We therefore mask out the pixels within 500 m of the major rupture trace and small areas that are apparently inconsistent with neighboring patches. The resulting interferogram is then tied to the GNSS observations to account for the possible shift of $2N\pi$ unwrapping ambiguity over the entire image. The resulting LoS displacements derived from the CSK data along three satellite tracks are shown in Figure 3. The overall deformation and magnitude are very similar to the Sentinel-1 results. The differences between the CSK and GNSS LoS displacements at the GNSS stations within the respective scenes are less than 2 cm for all three tracks.

In addition to the LoS displacements from the interferometric phase, we also derive the surface displacements along the satellite's azimuthal direction from the CSK data using a pixel tracking technique. For each aligned image pair, we divide the images into 1500 by 2000 patches along range and azimuth directions, respectively; each have a window size of 64×64 pixels. We then compute the upsampled cross correlation of radar amplitudes of each patch pair in the Fourier domain
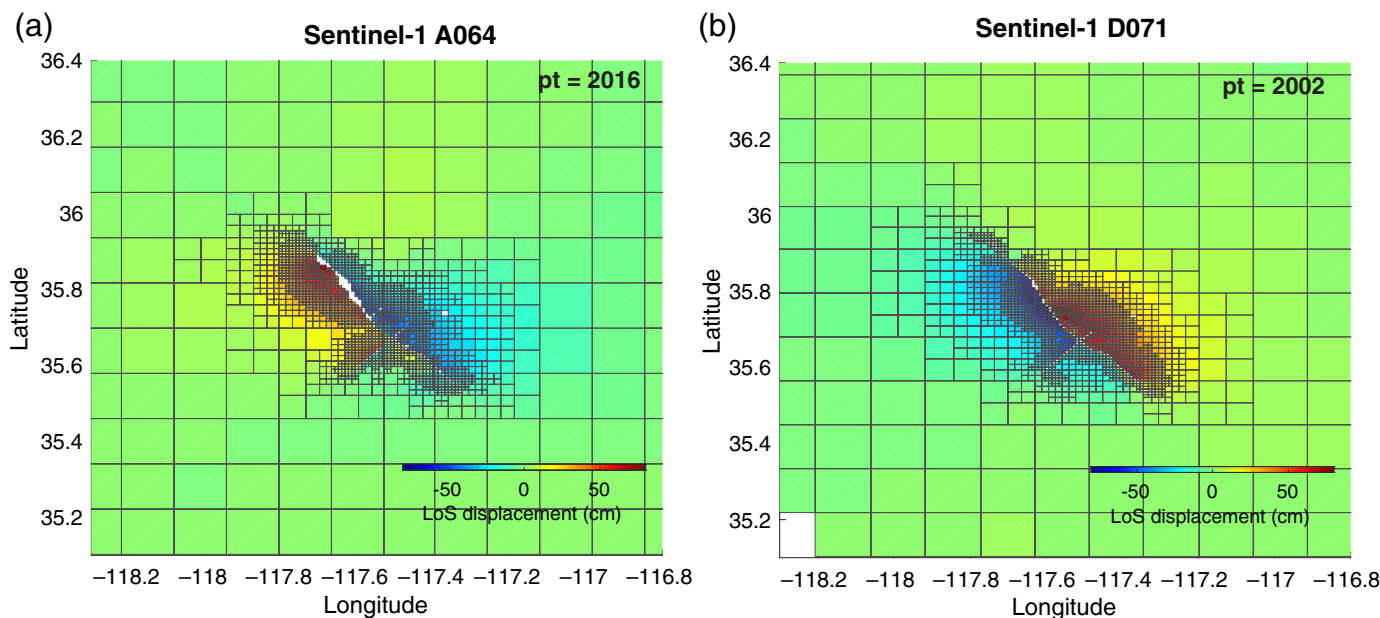
to find the shift between them at a subpixel accuracy (Guizar-Sicairos *et al.*, 2008). The output azimuthal offset map is filtered with a Gaussian filter of a 300-m wavelength, after masking out the patches of apparently low signal-to-noise ratio in the cross correlation. The resulting azimuthal offset map exhibits some ramp-like variations in the far field, which is likely due to the image misalignment. To correct for these artifacts, we use a slip model that is derived from the Sentinel-1 data to compute a synthetic azimuthal offset map for each CSK track (Wang and Bürgmann, 2019). We then use the observed offset values at pixels whose model predictions are smaller than 30 cm, in order to estimate a bilinear function, which is eventually removed from the entire offset map.

Figure 4. Azimuthal offsets derived from CSK data along the (a) ascending track Asc1 and (b) descending track Des1. Scenes from Asc2 only cover the southern half of the rupture, which largely overlap with Asc1 (Fig. 3b), so results from this track are not shown. Colored triangles represent the GNSS displacements projected onto the satellites' azimuthal directions. The differences of the azimuthal displacements derived from GNSS and CSK data are less than 15 cm at the GNSS stations. Fault-parallel motions along transects A–A′ (near the M_w 7.1 epicenter) and B–B′ are shown in (c) and (d), respectively. Red arrow (in panel d) marks the location of an eastern fault strand that was possibly involved in both the M_w 6.4 foreshock and the M_w 7.1 mainshock. Note that the offset across this fault strand reaches over 1 m. The color version of this figure is available only in the electronic edition.
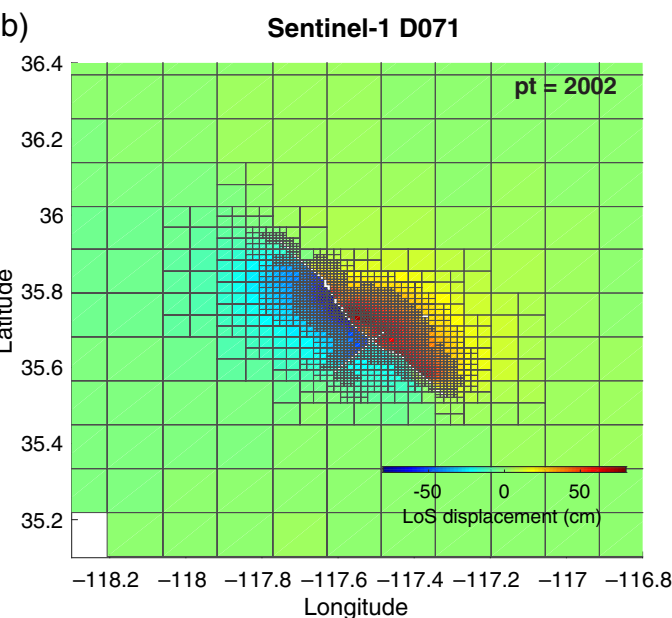
The resulting azimuthal offsets derived from the CSK data are shown in Figure 4. Compared to the LoS displacements derived from interferometric phase, measurements of the range or azimuthal offsets from pixel tracking are much noisier. Nonetheless, the data from all three CSK tracks show significant displacements across multiple fault strands. In particular, results from the ascending track Asc1 clearly reveal the surface deformation across much of the rupture extent. As the angle between the average strike of the M_w 7.1 rupture and the satellite path is 20°–30°, the azimuthal offset map shown in Figure 4 is a close proxy of the fault-parallel motion. Assuming an average fault strike of 325°, we estimate that the maximum surface slip

(a)   **(b)**

Figure 5. Downsampling of the Sentinel-1 LoS displacements using a model-aided quadtree downsampling scheme (Wang and Fialko, 2015) for the (a) ascending track A064 and (b) descending track D071. Rectangles show the areas within which the LoS displacements are averaged. The color version of this figure is available only in the electronic edition.

near the M_{w} 7.1 epicenter is 4.5 m (Fig. 4c), a result that is in good agreement with the field survey measurements (D. Ponti et al., unpublished manuscript, 2019, see Data and Resources).
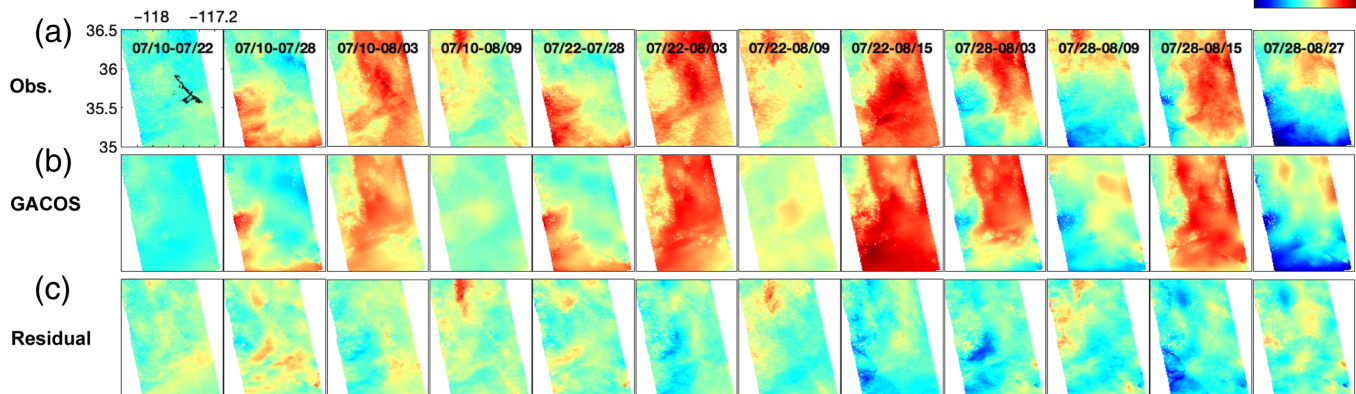
Data downsampling

High-resolution geospatial grid files of SAR and InSAR products are preferable for examining the details of a deformation field, but they are impractical for modeling purposes. Moreover, InSAR observations are intrinsically spatially correlated. To reduce the redundancy and facilitate the modeling, the original high-resolution interferograms must be downsampled. A common method known as quad-tree downsampling is used here to sample the image recursively, according to the gradient of the data variation (e.g., Jónsson et al., 2002). This algorithm works well for data of low-noise levels, but it may oversample data in areas with large phase gradients due to noise (atmospheric delays, decorrelation, unwrapping errors, etc.). To overcome this problem, we sample the InSAR and pixel offset data iteratively using model predictions (Wang and Fialko, 2015). An initial slip model is estimated from the inversion of coarsely sampled data, which is then used to compute synthetic interferograms or pixel offset maps. We then sample the synthetic interferograms and azimuthal offset maps, in order to obtain the bounding coordinates of each resolution cell (bin), which will be used to sample the real data. We note that this method is similar to the resolution-based downsampling scheme proposed by Lohman and Simons (2005). Figure 5 shows the downsampled Sentinel-1 LoS displacement using this method. The smallest cell size of our sampling is ~500 m, and the largest cell size is ~15 km. In the online data repository associated with this article, we provide the downsampled data of both Sentinel-1 and CSK LoS displacements and CSK azimuthal offset measurements in the format of ASCII files.

Early postseismic deformation

In this article, we also document the early postseismic deformation following the 2019 Ridgecrest earthquakes that was derived from both Sentinel-1 and CSK data. Compared to the coseismic deformation, signals of postseismic deformation due to the 2019 Ridgecrest earthquakes are much smaller (on the order of a few centimeters). Atmospheric phase delays due to water vapor variations in the troposphere over the study area, however, are as large as a few decimeters (Fig. 6). Therefore, to obtain clean and robust postseismic deformation measurements with InSAR, one must correct for or mitigate the atmospheric delays. We find that in southern California, range changes predicted by certain weather models match the Sentinel-1 interferograms reasonably well at relatively long-spatial wavelengths (e.g., >10 km). Particularly, the long-wavelength variations in many postseismic Sentinel-1 interferograms along the ascending track A064 resemble the Generic Atmospheric Correction Online Service for InSAR (GACOS) model predictions (Yu et al., 2018) well (Fig. 6). We therefore correct for the atmospheric noise in the postseismic interferograms of the ascending track A064 using GACOS. We stack the residual interferograms to obtain an average velocity, which is then used to compute the cumulative postseismic deformation during the observation period (from 10 July to 2 September 2019 for the ascending track A064). We note that, although the GACOS models can effectively reduce the large-scale variations of most

Figure 6. (a) Postseismic interferograms along the Sentinel-1 ascending track A064. Note that most interferograms contain significant noise due to atmospheric perturbations. (b) Tropospheric phase delays predicted by GACOS models. (c) Residual interferograms that are used for stacking. Because of space limitations, not all interferograms are shown. The color version of this figure is available only in the electronic edition.

interferograms along the Sentinel-1 ascending track A064 (acquisition time ∼06.51 p.m. PDT), they do not perform well for the descending track D071 (acquisition time ∼06.52 a.m. PDT). Thus, no atmospheric corrections are applied for the postseismic interferograms along the Sentinel-1 descending track D071.

The CSK acquisitions are rather irregular in time, and there are 2–3 postseismic acquisitions along each track before the end of August 2019. Similar to the Sentinel-1 interferograms, most of the CSK interferograms are significantly contaminated by atmospheric noise. Only a few CSK postseismic interferograms show clear fringe patterns that can be easily identified as postseismic deformation that is related to the 2019 Ridgecrest earthquake sequence. Therefore, instead of stacking multiple interferograms, we select the CSK interferograms whose phase is less variable in the relatively far field.

Figure 7 shows the cumulative postseismic deformation during the first ∼1–2 months after the 2019 Ridgecrest earthquake. The LoS displacements derived from both Sentinel-1 and CSK data along the ascending tracks are characterized by significant range decrease northwest of the M_w 7.1 epicenter, and moderate range decrease west of the fault junction between the M_w 6.4 and the M_w 7.1 ruptures. The maximum postseismic deformation along the LoS of the ascending satellite tracks exceeds 5 cm northwest of the M_w 7.1 epicenter. Range changes derived from Sentinel-1 data of the descending track D071, however, are mostly distributed east of the rupture trace, near the M_w 7.1 epicenter.

Discussion

The M_w 6.4 foreshock on 4 July was preceded by numerous foreshocks that took place northwest of its hypocenter (Huang *et al.*, 2019; Ross *et al.*, 2019). The M_w 6.4 foreshock also generated abundant aftershocks prior to the M_w 7.1 mainshock, illuminating a northwest-striking structure that extends roughly from the M_w 6.4 epicenter to the M_w 7.1 epicenter. The distributions of both fore- and aftershocks of the M_w 6.4 earthquake prior to the M_w 7.1 mainshock therefore indicate that the M_w 6.4 event possibly involved two nearly

orthogonal faults that struck northwest and southwest, respectively. Cross correlation of high-resolution optical images spanning only the M_w 6.4 event, however, rules out surface slip of >15 cm on the northwest-striking segment (Milliner and Donnellan, 2019). Our CSK pixel offset map clearly reveals surface offset across a northwest-striking fault strand that is located 2–3 km east of the major rupture trace. The surface slip across this fault strand could be up to ∼1 m (Fig. 4d). If the M_w 6.4 rupture did involve this fault segment, its slip must have been moderate and relatively deep. The clear surface offset across this fault would then indicate that this fault might have ruptured twice, with more pronounced and shallow slip during the M_w 7.1 mainshock. We note that this statement does not necessarily contradict Ross *et al.* (2019), who suggest that "no fault ruptured the same area twice", as the slip on this fault segment likely concentrated at different depths during the M_w 6.4 and the M_w 7.1 events.

As previously noted, postseismic deformation ∼2 months following the Ridgecrest earthquake seems to be quite asymmetrical across the fault trace. Specifically, for both Sentinel-1 and CSK data along the ascending tracks, the largest postseismic deformation concentrates to the west of the fault trace near the M_w 7.1 epicenter, whereas for the Sentinel-1 descending track, most of the range change appears distributed east of the fault trace. Such deformation patterns are qualitatively consistent with what one would expect from right-lateral strike-slip motion (i.e., afterslip). On the other hand, the concentration of postseismic deformation near the M_w 7.1 epicenter is located in an area where the rupture steps over to form a releasing bend. Coseismic pore-pressure decrease in the vicinity
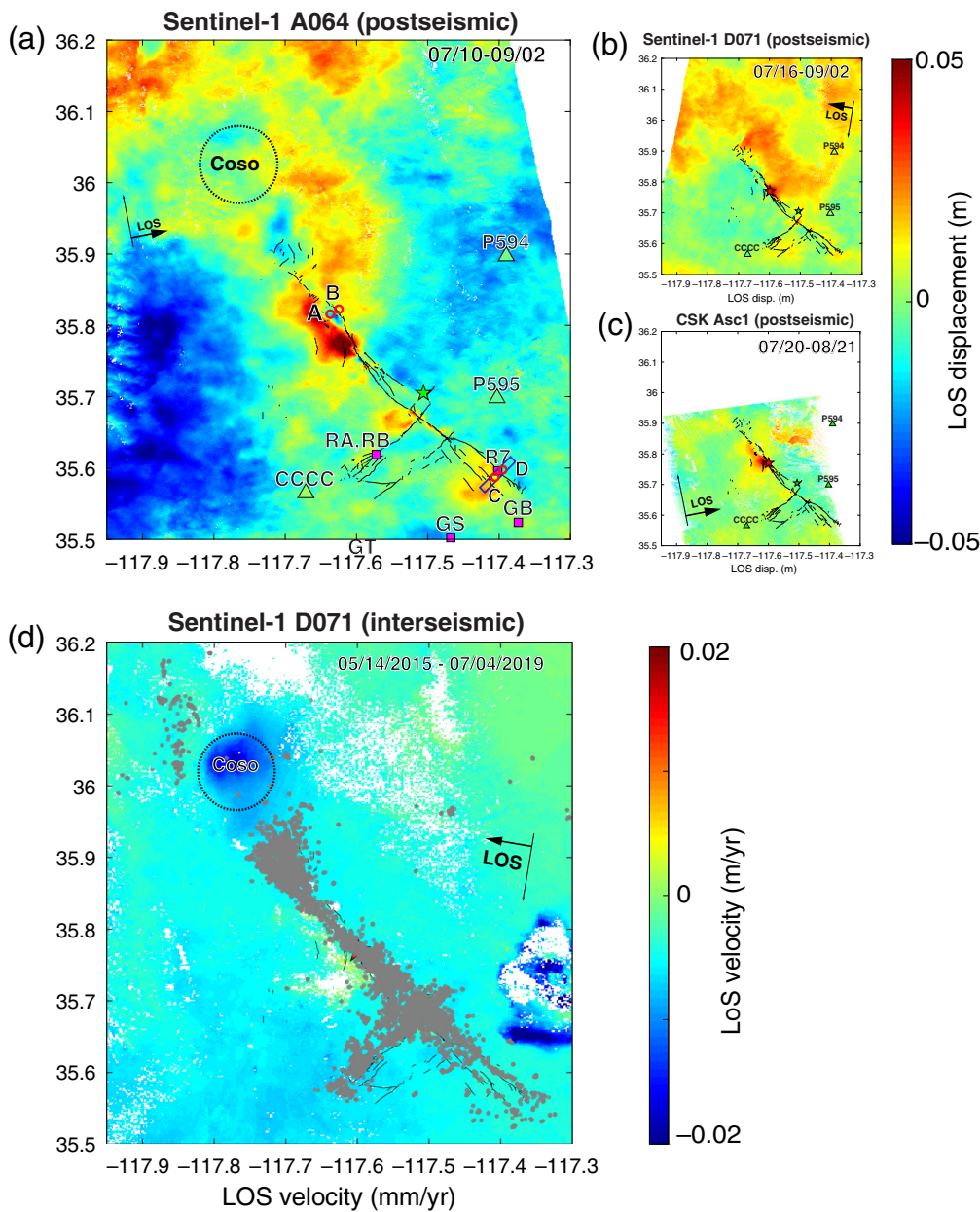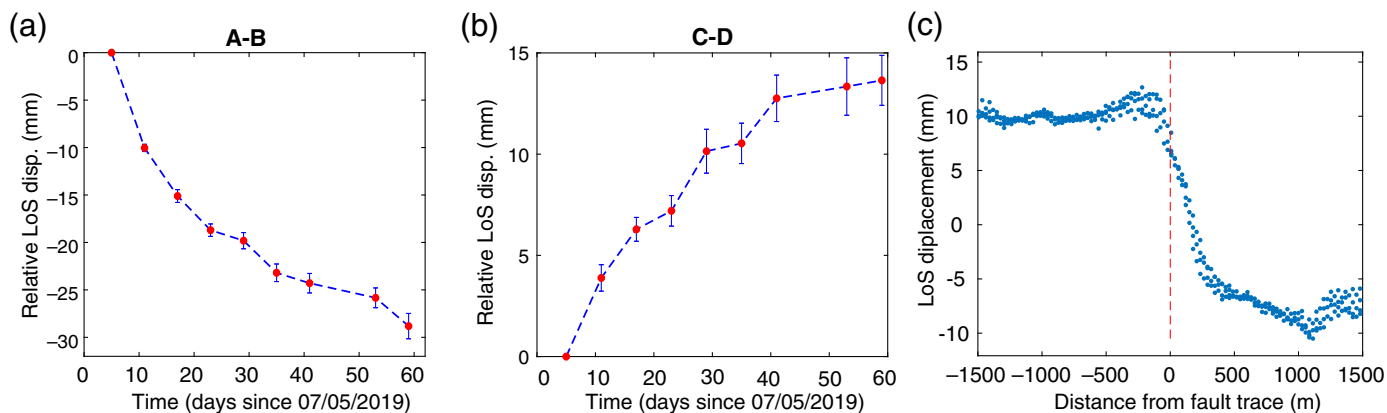
Figure 7. Postseismic and interseismic deformation around the 2019 Ridgecrest earthquake sequence. (a–c) Cumulative LoS displacements during the respective postseismic InSAR observation periods of Sentinel-1 (a,b) and CSK (c) acquisitions. For Sentinel-1, the results are obtained by stacking all postseismic interferograms of temporal baselines ≤30 days. For CSK data, because of the sparse data acquisitions, only a small number of postseismic interferograms exist that show clear fringe patterns that can be associated with the Ridgecrest ruptures. Magenta squares in (a) represent the creepmeters in Bilham and Castillo (2019). Triangles represent the PBO GNSS stations, color-coded by their cumulative postseismic displacements during the InSAR observation period projected onto the LoSs. Text labels in top right corner of each panel show the observation period of the respective tracks. (d) Interseismic deformation rate derived from Sentinel-1 data ~4 yr preceding the 2019 Ridgecrest earthquake sequence, to highlight the ground subsidence related to the Coco geothermal activities. Gray dots represent relocated aftershocks from the occurrence of the M_w 6.4 foreshock (15:33:49 UTC on 4 July 2019) to 09:00 UTC on 11 September 2019 (Huang *et al.*, 2019). The color version of this figure is available only in the electronic edition.

of this releasing bend may result in fluid migration toward this area after the earthquake, so that the fluid pressure in the crust can be re-equilibrated. This process, known as the poroelastic rebound (Peltzer *et al.*, 1998), may produce surface deformation that resembles the observed postseismic deformation in this study. Another intriguing observation is that the concentration of range decrease northwest of the M_w 7.1 epicenter, seen by the ascending track observations, seems to be separated by a smaller zone of range increase from the main rupture trace (around the red circle A in Fig. 7a). The observed postseismic deformation near the M_w 7.1 epicenter, therefore, appears to be rather complicated. Quantitative modeling of the postseismic deformation is beyond the scope of this study and will be described in a future paper.

There is little postseismic deformation near the Coso geothermal field (Fig. 7a), consistent with modest aftershock activity in this area (Fig. 7d, Ross *et al.*, 2019). However, we note that the current postseismic InSAR data presented in this article may still contain strong atmospheric noise at relatively long wavelengths, as the GNSS measurements at a few PBO stations within the InSAR scenes only show moderate postseismic deformation (e.g., less than 5 mm LoS displacement) during the respective InSAR observation periods, whereas the Sentinel-1 observations from both ascending and descending tracks show up to 2–3 cm range change around these GNSS stations. (Fig. 7). Future acquisitions will be

Figure 8. Time-dependent afterslip along the M_W 7.1 rupture. (a, b) Time series of the relative displacements between neighboring pixels across the fault at two locations. (c) Transect of postseismic LoS displacements across the fault near creepmeter R7 (Bilham and Castillo, 2019). The locations of the pixel pairs and the transect are shown in Figure 7a as red circles and a blue rectangle, respectively. Data shown are from Sentinel-1 ascending track A064 data collected between 10 July 2019 and 2 September 2019. The color version of this figure is available only in the electronic edition.

important to better constrain the postseismic deformation in the far field. For the same reason, the time series of the postseismic deformation are also quite noisy, so we do not provide them as the standard-alone products of this article. Interested readers are encouraged to contact the authors, because we anticipate to keep updating the results with more acquisitions.

Nevertheless, the relative displacement history between neighboring pixels is robust enough for us to examine the overall decaying rate of the postseismic deformation following the Ridgecrest earthquakes, since the atmospheric noises cancel out when pixels are close. Figure 7a shows the time series of relative LoS displacements between two points (A and B in Fig. 6a) of ∼300 m apart across the main rupture trace derived from Sentinel-1 data along the ascending track A064. The time series shows that the postseismic near-fault deformation associated with the 2019 Ridgecrest earthquake sequence rapidly decays with time. We also examine the relative displacements between two points across the fault near the southern end of rupture (C and D in Fig. 6a), near the creepmeter R7 in Bilham and Castillo (2019). Similar to the pair between A and B, the relative LoS displacements between these two points are characterized by rapid decay of deformation rate with time. During the observation period from 10 July to 2 September, the relative LoS displacement between these two points reaches ∼12 mm (Fig. 8), which corresponds to ∼35 mm of fault-parallel motion, assuming that the postseismic deformation here is dominated by horizontal motion. The cumulative LoS displacements along a profile perpendicular to the fault at this location suggest that the postseismic deformation here is distributed within a finite width of 500–1000 m (Fig. 8c). The inferred strain across this distributed shear zone is comparable to the near-fault short-baseline (∼5 m) extensometer measurements by Bilham and Castillo (2019). Our early postseismic InSAR data show no clear evidence of postseismic creep along the Garlock fault, which is consistent with the creepmeter measurements by Bilham and Castillo (2019).

Conclusions

The 2019 Ridgecrest earthquake sequence ruptured a series of conjugate faults in the broad eastern California shear zone

north of the Mojave Desert in southern California. In this article, we derive the coseismic displacements due to these ruptures using both C-band Sentinel-1 and X-band CSK SAR data that span both the M_W 6.4 foreshock and the M_W 7.1 mainshock. The LoS displacements derived from the interferometric phase of both Sentinel-1 and CSK data spanning the earthquakes agree well with GNSS measurements at PBO stations in the epicentral area. In addition to the LoS displacements, we also derive the coseismic displacement that is due to the 2019 Ridgecrest earthquake sequence along the CSK satellite's azimuthal direction, with pixel tracking of the fine-resolution data. Both the LoS phase measurements and the azimuthal offset maps clearly show that the M_W 6.4 foreshock and the M_W 7.1 mainshock have ruptured to the surface, with a maximum surface slip of ∼4.5 m on a northwest-striking rupture near the M_W 7.1 epicenter. The CSK azimuthal offset map also reveals a sharp offset of ∼1 m across a second northwest-striking fault strand that is 2–3 km east of the main rupture trace that was possibly involved in both the M_W 6.4 foreshock and the M_W 7.1 mainshock. Observed slip on a southwest-striking conjugate fault segment of ∼1.3 m likely occurred during the M_W 6.4 foreshock. In addition to the coseismic displacements, we also document early postseismic deformation associated with the 2019 Ridgecrest earthquake sequence with both Sentinel-1 and CSK data. The maximum postseismic deformation near the M_W 7.1 epicenter ∼2 months after the mainshock reaches over 5 cm along the satellites' lines of sight. The observed postseismic deformation is indicative of both afterslip and poroelastic rebound near the fault. Future SAR acquisitions from both sensors

will further improve the postseismic deformation measurements of the 2019 Ridgecrest earthquake. We provide data derived in this study in various data formats, which will be useful for a broad community studying this earthquake sequence.

Data and Resources

Coseismic deformation data derived in this study are available at https://zenodo.org/record/3475633#.XZvOSudKh7M (last accessed January 2020). The tarball file contains the coseismic surface deformation measurements due to the 2019 Ridgecrest earthquakes derived from interferometry of both Sentinel-1 and COSMO-SkyMed (CSK) and pixel tracking of the CSK data. The line of sight (LoS) and azimuthal displacements of both satellites are provided in downsampled ASCII files, as well as in high-resolution Network Common Data Form (NetCDF) and Geographic Tagged Image File Format (GeoTiff). The files include los_disp_ll.grd/los_disp_ll.tiff, which includes high-resolution LoS displacements in NetCDF or GeoTiff formats. los_downsample.txt includes downsampled LoS displacement in ASCII file format. azo_ll.grd/azo_ll.tiff includes azimuth displacement derived from the pixel tracking of CSK data in NetCDF or GeoTiff formats. los_downsample.txt includes downsampled azimuth displacement in ASCII file format. The 4–6 columns of the downsampled data describe the unit vectors (ve, vn, vz) of the LoS and the azimuth directions of the satellites' paths; therefore, LoS or Azimuthal displacements = Ue × ve + Un × vn + Up × vz, in which Ue, Un, and Up represent the ground deformation along the east, north, and vertical (positive for up) directions, respectively; ve, vn, and vz are east, north, and vertical components of the LoS or the satellite's flying path, respectively. Global Navigation Satellite System (GNSS) data used in this study are from Scripps Orbit and Permanent Array Center (SOPAC) (http://sopac-csrc.ucsd.edu/, last accessed September 2019). The Sentinel-1 Single Look Complex (SLC) data are downloaded from the Alaska Satellite Facility (ASF). CSK data come from Agenzia Spaziale Italiana, made available free-of-charge through the Geohazard Supersites and Natural Laboratories (GSNL) initiative San Andreas Fault Natural Laboratory which operates under the auspices of the Group on Earth Observations and the Committee on Earth Observing Satellites. Fault traces used in this study are from a Southern California Earthquake Center (SCEC) response page at https://response.scec.org/node/395?page=4 (last accessed September 2019). This dataset is also submitted to the *SRL* Data Mine section related to the 2019 Ridgecrest earthquakes. The unpublished manuscript by D. Ponti *et al.*, "Documentation of surface fault rupture and ground deformation features produced by the Ridgecrest M6.4 and M7.1 earthquake sequence of July 4 and 5, 2019," submitted to *Seismol. Res. Lett.*

Acknowledgments

References

Bilham, R., and B. Castillo (2019). Triggered slip and afterslip in the July 2019 Ridgecrest earthquake sequence, *Seismol. Res. Lett.* doi: 10.1785/0220190293.

Bürgmann, R., P. Rosen, and E. Fielding (2000). Synthetic Aperture Radar Interferometry to measure Earth's surface topography and its deformation, *Annu. Rev. Earth Planet. Sci.* **28,** 169–209.

Chen, C. W., and H. A. Zebker (2001). Two-dimensional phase unwrapping with use of statistical models for cost functions in nonlinear optimization, *J. Opt. Soc. Am.* **18,** no. 2, 338–351, doi: 10.1364/JOSAA.18.000338.

Fialko, Y., M. Simons, and D. Agnew (2001). The complete (3-D) surface displacement field in the epicentral area of the 1999 MW7.1 Hector Mine Earthquake, California, from space geodetic observations, *Geophys. Res. Lett.* **28,** no. 16, 3063–3066, doi: 10.1029/2001GL013174.

Fielding, E. J., Z. Liu, O. Stephenson, M. Zhong, C. Liang, A. Moore, S. Yun, and M. Simons (2019). Surface deformation related to the 2019 M_w 7.1 and M_w 6.4 Ridgecrest earthquakes in California from GPS, SAR interferometry, and SAR pixel offsets, *Seismol. Res. Lett.*, doi: 10.1785/0220190302.

Floyd, M., G. Funning, Y. Fialko, R. Terry, and T. Herring (2019). Survey and continuous GNSS in the vicinity of the July 2019 Ridgecrest earthquakes, *Seismol. Res. Lett.* doi: 10.1785/0220190234.

Guizar-Sicairos, M., S. Thurman, and J. Fienup (2008). Efficient subpixel image registration algorithms, *Optic. Lett.* **33,** no. 2, 156–158, doi: 10.1364/OL.33.000156.

Huang, H., R. Bürgmann, L. Meng, K. Wang, and B. Rousset (2019). Spatio-temporal foreshock evolution of the 2019 M 6.4 and M 7.1 Ridgecrest, California earthquakes, *Poster Presentation at 2019 SCEC Annual Meeting*, Palm Springs, California, 8–11 September 2019, SCEC Contribution 9723.

Jónsson, S., H. Zebker, P. Segall, and F. Amelung (2002). Fault slip distribution of the 1999 Mw 7.1 Hector Mine, California, earthquake, estimated from satellite radar and GPS measurements, *Bull. Seismol. Soc. Am.* **92,** no. 4, 1377–1389, doi: 10.1785/0120000922.

Lohman, R. B., and M. Simons (2005). Some thoughts on the use of InSAR data to constrain models of surface deformation: Noise structure and data downsampling, *Geochem. Geophys. Geosys.* **6,** Q01007, doi: 10.1029/2004GC000841.

Milliner, C. W. D., and A. Donnellan (2019). Using daily observations from Planet Labs satellite imagery to separate the surface deformation between the July 4th Mw 6.4 foreshock and July 5th Mw 7.1 mainshock during the 2019 Ridgecrest earthquake sequence, *Seismol. Res. Lett.* doi: 10.1785/0220190271.

Peltzer, G., P. Rosen, F. Rogez, and K. Hudnut (1998). Poroelastic rebound along the Landers 1992 earthquake rupture, *J. Geophys. Res.* **103,** no. B12, 30,131–30,145, doi: 10.1029/98JB02302.

Ross, Z. E., B. Idini, Z. Jia, O. L. Stephenson, M. Zhong, X. Wang, Z. Zhan, M. Simons, E. J. Fielding, S.-H. Yun, *et al.* (2019). Hierarchical interlocked orthogonal faulting in the 2019 Ridgecrest earthquake sequence, *Science* **366,** no. 6463, 346–351, doi: 10.1126/science.aaz0109.

Sandwell, D., R. Mellors, X. Tong, M. Wei, and P. Wessel (2011). Open radar interferometry software for mapping surface deformation, *Eos Trans. AGU* **92,** no. 28, doi: 10.1029/2011EO280002.

Wang, K., and R. Bürgmann (2019). Modeling of co- and early post-seismic deformation due to the 2019 Ridgecrest earthquake sequence, *Poster Presentation at 2019 SCEC Annual Meeting*, Palm Springs, California, 8–11 September 2019, SCEC Contribution 9887.

Wang, K., and Y. Fialko (2015). Slip model of the 2015 Mw 7.8 Gorkha (Nepal) earthquake from inversions of ALOS-2 and GPS data, *Geophys. Res. Lett.* **42,** no. 18, 7452–7458, doi: 10.1002/2015GL065201.

Wang, K., H. S. MacArthur, I. Johanson, E. K. Montgomery-Brown, M. P. Poland, E. C. Cannon, M. A. d'Alessio, and R. Burgmann (2019). Interseismic quiescence and triggered slip of active normal faults of Kīlauea Volcano's South Flank during 2001–2018, *J. Geophys. Res.* **84,** no. 13, 7616–7615, doi: 10.1029/2019JB017419.

Xu, X., and D. Sandwell (2019). Coseismic displacements and surface fractures from Sentinel-1 InSAR: 2019 Ridgecrest earthquakes, *Seismol. Res. Lett.* doi: 10.1785/0220190275.

Xu, X., D. T. Sandwell, E. Tymofyeyeva, A. González-Ortega, and X. Tong (2017). Tectonic and anthropogenic deformation at the Cerro Prieto geothermal step-over revealed by Sentinel-1A InSAR, *IEEE Trans. Geosci. Remote Sens.* **55,** no. 9, 5284–5292.

Yu, C., Z. Li, N. P. Pnna, and P. Crippa (2018). Generic atmospheric correction model for Interferometric Synthetic Aperture Radar observations, *J. Geophys. Res.* **123,** 9202–9222, doi: 10.1029/2017JB015305.